Modeling Magnetic Torque and Force for Controlled Manipulation of Soft-Magnetic Bodies

Jake J. Abbott, Olgaç Ergeneman, Michael P. Kummer, Ann M. Hirt, and Bradley J. Nelson

Abstract—**We calculate the torque and force generated by an arbitrary magnetic field on an axially symmetric soft-magnetic body. We consider the magnetization of the body as a function of the applied field, using a continuous model that unifies two disparate magnetic models. The continuous torque and force follow. The model is verified experimentally, and captures the often neglected region between weak and saturating fields, where interesting behavior is observed. We provide the field direction to maximize torque for a given field magnitude. We also find an absolute maximum torque, for a given body geometry and material, which can be generated with relatively weak applied fields. This paper is aimed at those interested in systems-level analysis, simulation, and real-time control of soft-magnetic bodies.**

Index Terms—**Ellipsoid, magnetic actuation, shape anisotropy, uniaxial symmetry, wireless microrobot.**

I. INTRODUCTION

One approach to the wireless control of microrobots is through externally applied magnetic fields [1]. These untethered devices could navigate bodily fluids for minimally invasive surgical and diagnostic procedures [2]–[5], or could be used as the end-effectors of micromanipulation systems [6], [7]. There is a significant body of work dealing with noncontact magnetic manipulation where the object to be manipulated is a permanent magnet [5], [7]–[9]. In these cases, the magnetization of the object is effectively independent of the applied magnetic field, and the object can be modeled as a simple magnetic dipole. The resulting equations for the torque and the force on the object in an applied field are straightforward. We are also interested in precise control of soft-magnetic objects. Soft-magnetic materials provide easier fabrication as well as different possibilities in control. In addition, soft-magnetic materials have the potential for levels of magnetization as high as the remanence magnetization of permanent magnets [10]–[12]. However, with soft-magnetic materials, the magnetization of the body is a nonlinear function of the applied magnetic field, and the relationship between the applied field and the resulting torque and force is nontrivial.

Many researchers have considered the control of soft-magnetic beads [3], [4], [13], where a spherical shape simplifies the control problem since there is no preferred direction of magnetization. Most of the basic results needed for precise magnetic control of nonspherical soft-magnetic bodies are available in the literature [11], [12], [14], [15], but the difficulty lies in the correct application of these existing results. As we consider prior work, we are confronted with multiple systems of units as well as multiple conventions for expressing the basic quan-

tities and governing equations for magnetization. We find that material parameters such as permeability and susceptibility are relatively constant and of practical use if the applied field is weak, but become field-dependent for stronger fields. The magnetization of a body has a saturation limit, and after this limit has been reached, the relationship between the applied field and the magnetization changes significantly. We find that many existing results rely on the calculation of the "internal" magnetic field, which is a function of both the applied magnetic field and the resulting demagnetizing field, and consequently, requires a proper application of additional results; this proper application is not clearly explained in existing texts. Magnetization in relatively low fields is typically treated completely separately from magnetization in higher fields, and there is essentially no discussion about the transition between these regions. In practice, finite element methods are often used to characterize the magnetization of magnetic materials, but these methods are impractical for application in real-time control.

In this paper, we provide a simple model for the magnetic torque and force on a small axially symmetric soft-magnetic body. By combining disparate magnetic models, we create a unified model that is continuous and accurate for any applied field. We show that the knowledge of material parameters such as permeability or susceptibility is relatively unimportant, as the determination of magnetic torque and force is dominated by body geometry and the saturation magnetization of the material. We provide the torque and force on the body as a simple input/output mapping of the applied field, without the need to calculate the internal field. We show that, for each applied field magnitude, there is an optimal field angle to maximize torque, and we provide the equation. Simply increasing the magnitude of the applied field is never an optimal strategy to maximize torque. We find that there is no theoretical limit to magnetic force, but the magnetic torque does have an upper bound that can be achieved with a finite and relatively low applied field.

One aspect of our model that is particularly important is continuity. For any given applied field, we can calculate the torque and force on the body as they change continuously with changes in the applied field. This continuity allows us to invert the model so that, for a given desired torque and force, we can calculate the necessary applied field (magnitude, direction, and gradients). This property is highly desirable for closed-loop control using magnetic fields that are likely to vary between saturating and nonsaturating strengths. By designing a control system that generates continuous desired torque and force trajectories, continuous desired applied-field trajectories will follow, and we will avoid the types of discontinuities that cause problems in any physical realization.

II. CONTINUOUS MAGNETIZATION MODEL

We consider a soft-magnetic body with a unique axis of symmetry, as shown in Fig. 1. We will explicitly consider ellipsoids, but it has been shown previously that many simple geometries can be accurately modeled magnetically as ellipsoids [16], [17]. The body coordinate frame is located at the center of mass with the X-axis aligned with the axis of symmetry. The body lies in an external magnetic field with a value $\mathbf{H}$ at the body's center of mass. The field magnetizes the body to a magnetization $\mathbf{M}$. Both $\mathbf{H}$ and $\mathbf{M}$ are vectors with units ampere per meter. Because of the symmetry of the body, the field $\mathbf{H}$, the magnetization $\mathbf{M}$, and the axis of symmetry are coplanar. It is also possible to express the applied magnetic field as an applied magnetic flux density $\mathbf{B}$ with units tesla (T), but this is related to $\mathbf{H}$ simply as $\mathbf{B} = \mu_0 \mathbf{H}$, where $\mu_0 = 4\pi \times 10^{-7}$ T·m/A is the permeability of free space.
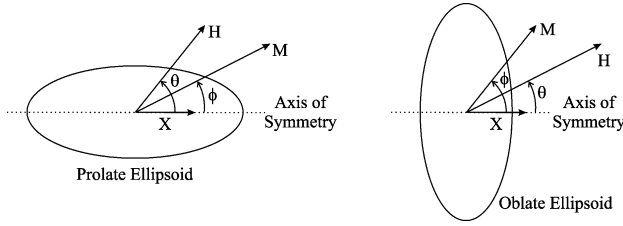
Fig. 1. Axially symmetric bodies in an external magnetic field. The X-axis of the body frame is aligned with the axis of symmetry. The field $\mathbf{H}$, the magnetization $\mathbf{M}$, and the axis of symmetry are coplanar. $\theta \in [0°, 90°]$ is the angle between H and the axis of symmetry, and $\phi \in [0°, 90°]$ is the angle between M and the axis of symmetry. If the axis of symmetry is the long axis of the body, it is referred to as the "easy axis," since it is the easiest direction to magnetize.

We assume a polycrystalline body with many randomly oriented grains, where the interaction of individual magnetic domains is neglected, as is the effect of magnetocrystalline anisotropy. Consequently, shape anisotropy is assumed to be the dominant factor in determining the magnetic energy; it has been noted in prior work that this is often a valid assumption. We assume that hysteretic effects are negligible, which is also valid for many soft-magnetic materials. The body is also assumed to be small relative to the local changes in the applied magnetic field, such that the field can be assumed to change linearly across the volume of the body. This assumption is used to ensure that magnetic effects, which are distributed across the volume of the body, can reasonably be approximated as a lumped effect at the center of mass of the body. In Section IV, we verify that this can be a safe assumption with real magnetic field sources and relatively large bodies.

We now develop a magnetization model with two distinct regions. In the first region, which is valid at low applied fields, the magnetization grows linearly with the applied field until it reaches a saturation magnitude. In the second region, the constant-magnitude saturated magnetization vector rotates toward the applied field asymptotically as the field's strength increases.

Let us first consider the linear-magnetization region, valid at relatively low applied fields. The magnetization is related to the internal field by the susceptibility of the material χ as $\mathbf{M} = \chi \mathbf{H}_i$. The internal field $\mathbf{H}_i$ is a function of the applied field $\mathbf{H}$, as well as a demagnetizing field: $\mathbf{H}_i = \mathbf{H} + \mathbf{H}_d$. The demagnetizing field is related to the magnetization by a tensor N of demagnetization factors based on the body geometry: $\mathbf{H}_d = -N\mathbf{M}$. The matrix N is diagonal if the body coordinate frame is chosen to align with the principle axes of the body: $N = \mathrm{diag}(n_x, n_y, n_z)$. Combining the earlier assumptions, we can relate the magnetization to the applied field by an apparent susceptibility tensor

$$\mathbf{M} = \mathcal{X}_a \mathbf{H} \tag{1}$$

with a tensor of the form

$$\mathcal{X}_a = \mathrm{diag}\left(\frac{\chi}{1 + n_x\chi}, \frac{\chi}{1 + n_y\chi}, \frac{\chi}{1 + n_z\chi} \right). \tag{2}$$

We must assert that $\mathbf{M}$, $\mathbf{H}$, and $\mathcal{X}_a$ are all written with respect to the body frame. Because of symmetry of the body, we need only consider two demagnetization factors: the factor along the axis of symmetry n_a and the factor in all radial directions perpendicular to the axis of symmetry n_r. If we then assume relatively large susceptibility values typical of soft-magnetic materials, typically on the order of 10^3–10^6, and we assume that the demagnetization factors are not too close to zero, we can approximate (2) with

$$\mathcal{X}_a = \mathrm{diag}\left(\frac{1}{n_a}, \frac{1}{n_r}, \frac{1}{n_r} \right). \tag{3}$$

That is, magnetization is insensitive to changes in susceptibility if the susceptibility is relatively high, and is instead dominated by body geometry. We can compute the magnetization angle ϕ directly, assuming (3), as

$$\phi = \tan^{-1}\left(\frac{n_a}{n_r} \tan\theta \right). \tag{4}$$

If the magnetization vector computed earlier results in $|\mathbf{M}| \leq m_s$, where m_s is the saturation magnetization of the material in ampere per meter, then we take $\mathbf{M}$ and ϕ as accurate. However, if we compute $|\mathbf{M}| > m_s$, then we move into the saturated-magnetization region. We set $|\mathbf{M}| = m_s$ and compute the rotation of $\mathbf{M}$ by minimizing the magnetic energy

$$e = \frac{1}{2}\mu_0 v(n_r - n_a)m_s^2 \sin^2\phi - \mu_0 v m_s |\mathbf{H}| \cos(\theta - \phi) \tag{5}$$

with respect to ϕ. The energy e has units of joule, and v is the volume of magnetic material in meter cube. This equation typically models the magnetic energy of a single-magnetic-domain sample, but it is a good approximation of a multidomain body once saturation has been reached. To minimize e in (5), $\mathbf{M}$ will rotate such that ϕ satisfies the transcendental equation

$$(n_r - n_a)m_s \sin(2\phi) = 2|\mathbf{H}| \sin(\theta - \phi). \tag{6}$$

The magnetization model developed above combines disparate magnetic models in a way that has not been done previously. Although continuity of the actual magnetization of the body would be expected, the continuity of the model is nontrivial, since each of the disparate magnetic models are simplifications of reality created under specific sets of assumptions. The magnitude of the magnetization is clearly continuous across the transition between models. Although it is not, at first, obvious, it is also possible to analytically demonstrate that the two models have a continuous transition in the magnetization angle ϕ. From (1) and (3), we can find, after some manipulation, the applied field magnitude that just saturates the material (i.e., the field magnitude at the transition between modeling regions)

$$|\mathbf{H}|_{\mathrm{sat}} = \frac{m_s n_a n_r}{\sqrt{n_a^2 \sin^2\theta + n_r^2 \cos^2\theta}}. \tag{7}$$

Note that the saturating field magnitude is dependent on the applied field angle θ. If we consider the governing equation of the saturation region (6), at the transitional field magnitude (7), we find, after some manipulation, that the magnetization angle (4) from the linear region does, in fact, satisfy (6). Consequently, with our combined model, the magnetization vector $\mathbf{M}$ does change continuously with changes in the applied field $\mathbf{H}$.

The demagnetization factors for general ellipsoidal bodies are computed in [18]. They are constrained by the relation $n_x + n_y + n_z = 1$, which we rewrite for an axially symmetric body as $n_a + 2n_r = 1$. The demagnetization factor for the axis of symmetry is computed for a prolate ellipsoid as

$$n_a = \frac{1}{R^2 - 1}\left(\frac{R}{2\sqrt{R^2 - 1}} \ln\left(\frac{R + \sqrt{R^2 - 1}}{R - \sqrt{R^2 - 1}} \right) - 1 \right) \tag{8}$$

and for an oblate ellipsoid as

$$n_a = \frac{R^2}{R^2 - 1}\left(1 - \frac{1}{\sqrt{R^2 - 1}} \sin^{-1}\left(\frac{\sqrt{R^2 - 1}}{R} \right) \right) \tag{9}$$

where $R \geq 1$ is the ratio of long and short dimensions of the body.

III. TORQUE AND FORCE

Once equipped with a model of the magnetization vector in the body frame, we can compute the torque and force on the body using the torque and force on a magnetic dipole in an external field. For both torque and force, continuity follows directly from the continuity of magnetization. The magnetization of an ellipsoidal body is uniform throughout, allowing us to consider the volume as contributing linearly to the torque and force.

Let us begin by considering magnetic torque, which tends to align the long dimension of the body with the applied field:

$$\mathbf{T} = \mu_0 v \mathbf{M} \times \mathbf{H} \tag{10}$$

in newton meter. At fields low enough such that $|\mathbf{M}| < m_s$, we can compute the magnitude of the torque analytically as

$$|\mathbf{T}| = \frac{\mu_0 v |n_r - n_a|}{2 n_a n_r} |\mathbf{H}|^2 \sin(2\theta). \tag{11}$$

The torque is quadratic in $|\mathbf{H}|$, and is maximized when $\theta = 45°$ for all $|\mathbf{H}| \le |\mathbf{H}|_{\text{low}}$, where

$$|\mathbf{H}|_{\text{low}} = \frac{m_s n_a n_r \sqrt{2}}{\sqrt{n_a^2 + n_r^2}}. \tag{12}$$

When the applied field is high enough such that $|\mathbf{M}| = m_s$, for a given θ, we find that the magnitude of the torque can be computed analytically as

$$|\mathbf{T}| = \frac{\mu_0 v |n_r - n_a|}{2} m_s^2 \sin(2\phi) \tag{13}$$

where ϕ is the solution of (6). We find that torque is no longer maximized when $\theta = 45°$, but rather when $\phi = 45°$. We must solve (6) to determine the applied field angle θ to maximize torque, and the solution will depend on $|\mathbf{H}|$. If the applied field is extremely high so that $\phi \approx \theta$, then (13) becomes the standard result used with torque magnetometers [15]. However, we arrived at this result without the typical assumptions (e.g., assuming $\mathbf{M}$ and $\mathbf{H}$ are parallel). At these very high fields, we again expect to maximize torque when $\theta \approx 45°$.

We find that the torque on a soft-magnetic body has an upper bound that does not depend on the applied field, and is only a function of the body geometry and saturation magnetization

$$|\mathbf{T}|_{\text{max}} = \frac{\mu_0 v |n_r - n_a| m_s^2}{2}. \tag{14}$$

It is interesting to note that the magnitude of the applied field has a large effect on the magnitude of the torque in the unsaturated region, yet after saturation, we must only know the magnitude of the applied field to correctly calculate the optimal angle to apply the field to generate $|\mathbf{T}|_{\text{max}}$. We are able to explicitly calculate a threshold field magnitude that we must apply to achieve $|\mathbf{T}|_{\text{max}}$

$$|\mathbf{H}|_{\text{high}} = m_s \sqrt{\frac{n_a^2 + n_r^2}{2}}. \tag{15}$$

This field must be applied at $\theta = \tan^{-1}(n_r/n_a)$ to achieve $|\mathbf{T}|_{\text{max}}$. It is possible to achieve $|\mathbf{T}|_{\text{max}}$ for any field $|\mathbf{H}| \ge |\mathbf{H}|_{\text{high}}$, but the field must be applied at the correct angle. This optimal angle θ always lies somewhere between $45°$ and $\tan^{-1}(n_r/n_a)$. It is important to note, and somewhat nonintuitive, that simply increasing the magnitude of the applied field will never tend toward the maximum possible torque $|\mathbf{T}|_{\text{max}}$; the field should be applied at a magnitude-specific angle.

There exists a range of applied-field magnitudes that are large enough to reach saturation but not large enough to simultaneously achieve $\phi = 45°$, but are also too large to use the simple assumption that torque is maximized at $\theta = 45°$. For these intermediate field magnitudes, the optimal field angle to maximize torque is found by solving (7) for θ, then ϕ is computed with (4) and $|\mathbf{T}|$ is computed with (13).

The result of the preceding analysis is a simple set of equations to choose the optimal angle to apply the magnetic field to develop as much torque as possible at a given field magnitude $|\mathbf{H}|$

$$\theta_{\text{opt}} = \begin{cases} 45°, & |\mathbf{H}| \le |\mathbf{H}|_{\text{low}} \\ \tan^{-1}\left(\frac{n_r}{n_a} \sqrt{\frac{|\mathbf{H}|^2 - m_s^2 n_a^2}{m_s^2 n_r^2 - |\mathbf{H}|^2}} \right), & |\mathbf{H}|_{\text{low}} \le |\mathbf{H}| \le |\mathbf{H}|_{\text{high}}, \\ \sin^{-1}\left(\frac{(n_r - n_a) m_s}{2 |\mathbf{H}|} \right) + 45°, & |\mathbf{H}|_{\text{high}} \le |\mathbf{H}|. \end{cases} \tag{16}$$

This optimal choice of θ changes continuously with $|\mathbf{H}|$. Again, it is only possible to generate $|\mathbf{T}|_{\text{max}}$ if $|\mathbf{H}| \ge |\mathbf{H}|_{\text{high}}$.

Let us now consider the force on a magnetic dipole

$$\mathbf{F} = \mu_0 v (\mathbf{M} \cdot \nabla) \mathbf{H} \tag{17}$$

in newton, where ∇ is the gradient operator

$$\nabla = \begin{bmatrix} \frac{\partial}{\partial x} & \frac{\partial}{\partial y} & \frac{\partial}{\partial z} \end{bmatrix}^T. \tag{18}$$

Since there is no electric current flowing through the region occupied by the body, Maxwell's equations provide the constraint $\nabla \times \mathbf{H} = \mathbf{0}$. This allows us to express (17), after some manipulation, in a more intuitive and useful form

$$\mathbf{F} = \mu_0 v \begin{bmatrix} \frac{\partial}{\partial x} \mathbf{H}^T \\ \frac{\partial}{\partial y} \mathbf{H}^T \\ \frac{\partial}{\partial z} \mathbf{H}^T \end{bmatrix} \mathbf{M}. \tag{19}$$

The magnetic force in a given direction is the dot product of: 1) the derivative of the field in that direction and 2) the magnetization. We find that, unlike torque, the magnetic force has no upper bound due to saturation. We can always generate larger forces by generating larger directional derivatives in the applied field.

There has been a great deal of interest in the control of soft-magnetic beads, and this special case of spherical geometry warrants special mention. Because there is no shape anisotropy, the magnetization vector $\mathbf{M}$ will always align itself with the applied field $\mathbf{H}$. A consequence is that no magnetic torque is generated on the bead. This also leads to a major simplification of the magnetic force in (19) that is only a function of the magnitude of the applied field

$$\mathbf{F} = \mu_0 v |\mathbf{M}| (\nabla |\mathbf{H}|). \tag{20}$$

In the low-field region where $|\mathbf{H}| \le m_s/3$, we can express the magnetization simply as $|\mathbf{M}| = 3|\mathbf{H}|$. In the high-field region, where $|\mathbf{H}| > m_s/3$, we have $|\mathbf{M}| = m_s$.

IV. EXPERIMENTAL VERIFICATION

To experimentally verify our model, we machined a prolate ellipsoid, shown in the inset of Fig. 2(a), that is 4.90 mm long and 2.54 mm wide from HyMu 80 (80% Ni, 14.48% Fe, 5% Mo, 0.5% Si, 0.02% Cu), which is a nearly ideal soft-magnetic material. The density of HyMu 80 is 8700 kg/m^3, and the mass was measured as 145.2 mg, giving a volume $v = 1.669 \times 10^{-8}$ m^3. With a length-to-width ratio of $R = 1.93$, (8) is used to compute $n_a = 0.180$ and $n_r = 0.410$.

Magnetization data were collected with a MicroMag 3900 vibrating-sample magnetometer (VSM) from Princeton Measurements Corporation. To obtain a baseline measurement of magnetic saturation to
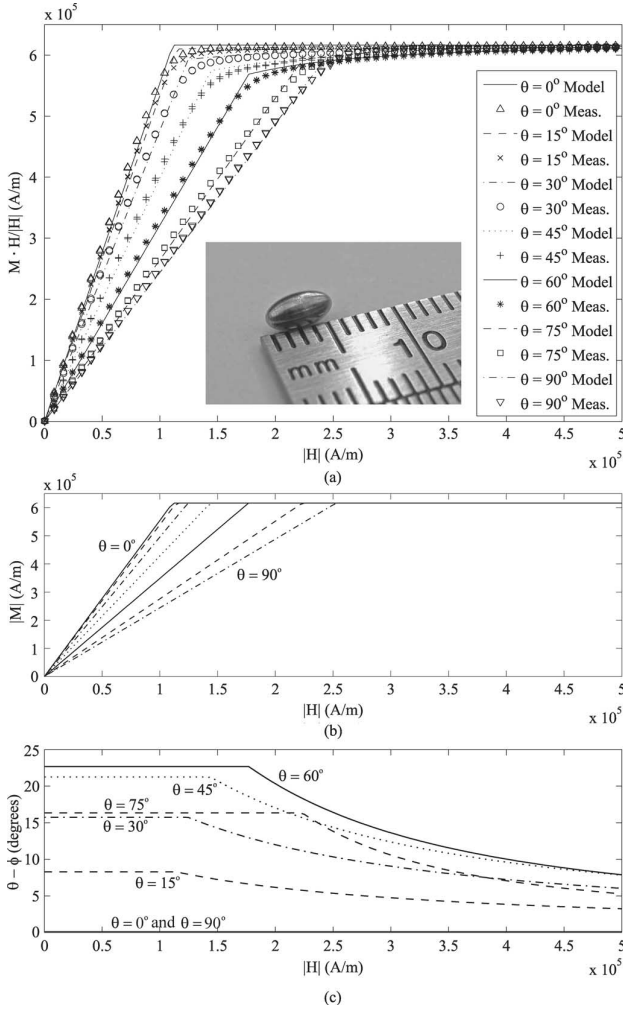
Fig. 2. Modeled and measured magnetization versus applied field strength for various applied field angles. (a) Experimental data of the component of the magnetization parallel to the applied field. (b) Inset shows the machined ellipsoid used in the experiments. The magnitude of magnetization predicted by the model. (c) Angle between the applied field and the predicted magnetization.
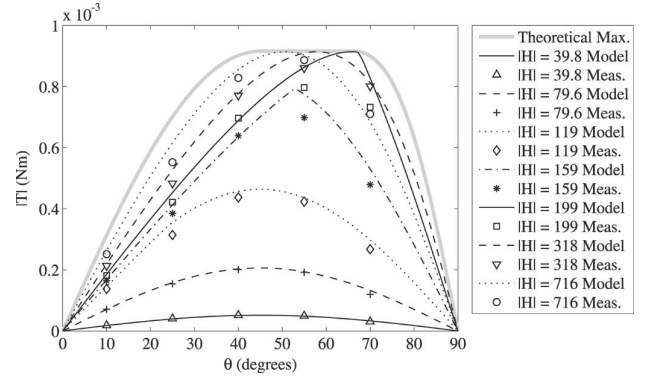

Fig. 3. Modeled and measured torque magnitude versus applied field angle for various applied field strengths. Field strength values are reported in kiloampere per meter.
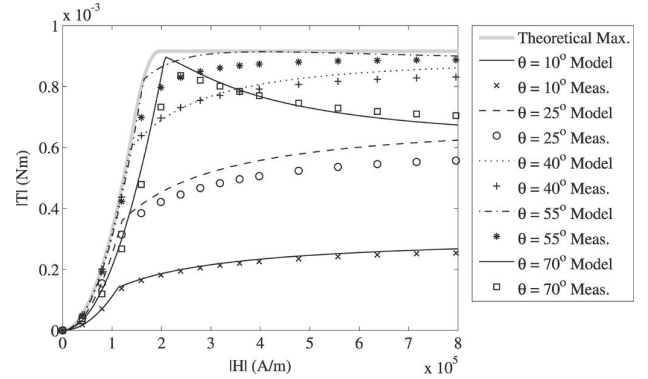

Fig. 4. Modeled and measured torque magnitude versus applied field strength for various applied field angles.

correct for the size effects of our relatively large ellipsoid, we obtained VSM data for a smaller, roughly spherical sample with a mass of 5.40 mg, resulting in a measured saturation magnetization of $m_s = 6.163 \times 10^5$ A/m.

Fig. 2(a) shows the magnetization model compared with the measured VSM data for our ellipsoid. It is evident that the magnetization model captures the true behavior. The corners in the actual data are smoother than that predicted by the model, which is expected with a model containing a discrete transition point. We also observe the continuity of the model in the transition between regions. Experimental data are shown for both increasing and decreasing applied fields; this is difficult to perceive in the plot, reinforcing the assumption that hysteretic effects are negligible. Fig. 2(b) and (c) provides an additional insight into the inner workings of the model. In the low-field region, the magnitude of the magnetization vector grows with no rotation until it saturates. As the field increases beyond saturation, the magnetization vector rotates toward the applied field. A common assumption used in magnetics is that the magnetization vector is parallel to the applied

field (i.e., $\phi = \theta$) at very high fields. From Fig. 2(c), our model predicts that this can be a poor assumption to make for certain geometries.

For example for our case: helixes!!!

Next, magnetic torque was measured with a custom-built torque magnetometer [19]. The torque data are compared with the model in Fig. 3, where constant-magnitude uniform fields are rotated with respect to the body. The same data set is presented in Fig. 4, but shown with the angle of the field with respect to the body held constant, and the magnitude varying. In each plot, we also include the theoretical maximum torque. The data confirm that our simple model captures the salient features of the magnetic torque across applied fields. Again, we would expect that sharp corners in the model would be smoothed out in the measured data. Other small errors in these plots are most likely accounted for by the imprecision in machining a perfect ellipsoid at this scale, as well as inaccuracies in the torque magnetometer. In each of these plots, we observe an interesting and nonintuitive behavior that is predicted by the model. We observe the shift in the optimal applied-field angle as we vary the field strength. We also see that, at certain applied-field angles, increasing the field magnitude actually decreases the torque. We find that the predicted values for $|\mathbf{T}|_{\max} = 9.16 \times 10^{-4}$ N·m and $|\mathbf{H}|_{\text{high}} = 1.95 \times 10^5$ A/m are good predictors of the measured values.

Finally, we measured the force on the machined ellipsoid due to the field of a permanent magnet, using a custom-built measurement system described in detail in [20]. The field along the dipole axis of the magnet is known accurately, and the force is measured with a precision scale as the ellipsoid is moved along the dipole axis. The
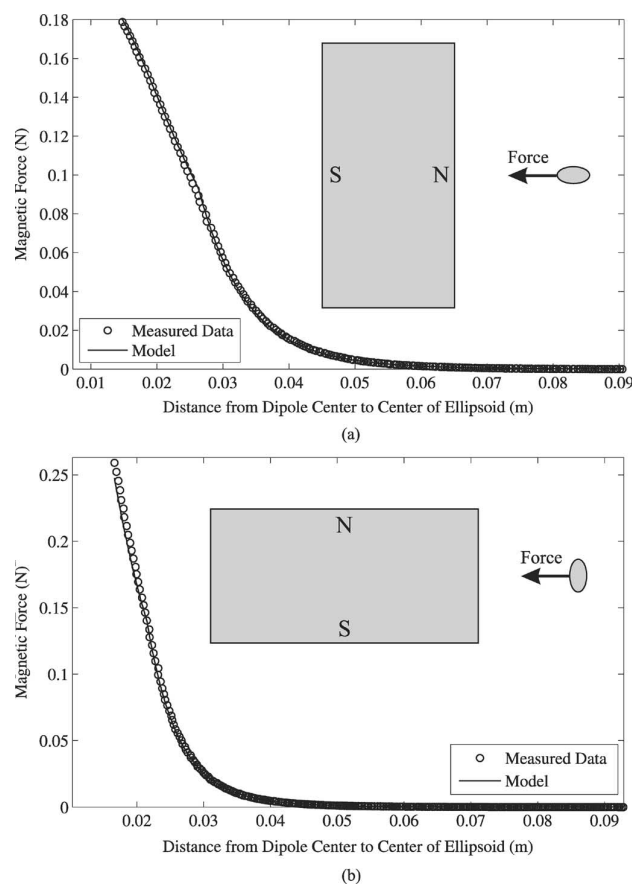
(a)

(b)

Fig. 5. Modeled and measured force magnitude versus distance from the dipole center, which lies below the magnet's surface. (a) Axial direction. (b) Lateral direction. The insets illustrate the experimental setup, drawn with a 1:1 scale to the data. The left edges of the plots correspond to the surface of the magnet.
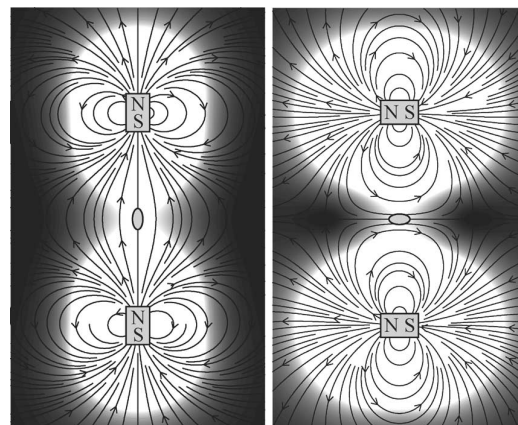

Fig. 6. Magnetic fields of two dipole pair configurations where pure torque is possible. Shading shows field magnitude, scaled to emphasize the points of interest, which are also shown by ellipsoids in their equilibrium orientation.
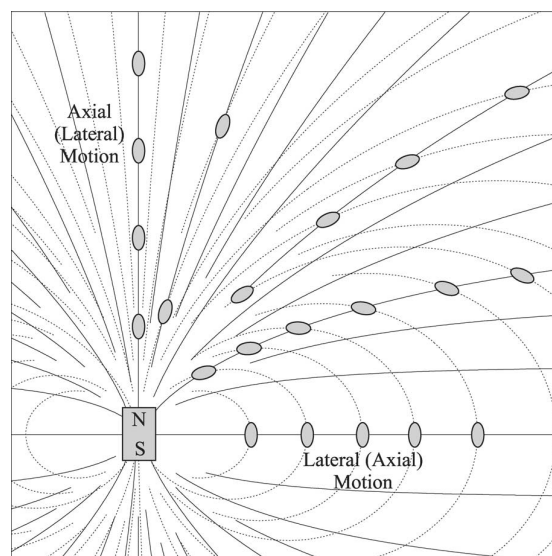

Fig. 7. Translation paths of a body as it is attracted to a magnetic dipole. Magnetic field lines are shown ($\cdots$). Force lines are also shown (——), assuming that the long dimension of the body is aligned with the field. The body will typically rotate as it is attracted toward the dipole, but pure axial and lateral translations of the body are possible, as shown for prolate (oblate) bodies.

long axis of the ellipsoid is perpendicular to the magnet's northern surface. Fig. 5(a) shows the measured magnetic force on the ellipsoid in the axial direction versus the value predicted by the model. The field to the side of the permanent magnet along a path perpendicular to the dipole axis is also known accurately. The force on the ellipsoid is measured along that path as well, with the long axis of the ellipsoid parallel to the dipole axis. Fig. 5(b) shows the measured magnetic force on the ellipsoid in the lateral direction versus the value predicted by the model. From Fig. 5, it is clear that the model captures the true force behavior, including the transition between linear and saturated magnetization regions, which appears as a corner in the data.

V. Discussion

Analysis of (10) and (19) shows that any point where $\mathbf{H} \neq \mathbf{0}$ and $\partial \mathbf{H}/\partial x = \partial \mathbf{H}/\partial y = \partial \mathbf{H}/\partial z = \mathbf{0}$ can be used to apply pure torques, and consequently, pure rotations, to a soft-magnetic body. Fig. 6 shows two magnetic dipole configurations that contain points that can be used to apply pure torques. The dipoles can be created by permanent magnets or electromagnets. The result of this type of magnetic manipulation is a 2-DOF pointing orientation movement of the body's axis of symmetry. The control of rotation about the axis of symmetry is not possible. Manipulation can be achieved by either rotating the dipole pair [2] or constructing sets of orthogonal dipoles [9]. Note that the pure-torque points seen in Fig. 6 correspond to unstable equilibria, so additional control (e.g., visual servoing) is needed to perform pure rotations.

Fig. 7 shows how our axially symmetric body will translate in the field of a magnetic dipole. The figure shows the dipole's magnetic field, superimposed with force field lines that assume that the body is aligned with the field (or is a sphere). We find that the body typically rotates as it translates toward the dipole. However, we find that pure axial and lateral movements of the body are possible along the dipole axis, and along any line through the dipole center and perpendicular to the dipole axis. These pure-translation movements correspond to the experimental data shown in Fig. 5. In addition to the assumption that the body is always aligned with the field, the force field lines in Fig. 7 were created assuming that the body never reaches magnetic saturation. If either of these two assumptions are violated, the force field lines will change, but the qualitative nature of Fig. 7 will remain.

VI. Conclusion

We have provided a simple model for magnetic torque and force on soft-magnetic bodies with axial symmetry. The model only requires the knowledge of body geometry and the saturation magnetization of the material. The model handles low and very high applied field intensities well, agreeing with existing models for those regions. In addition and most importantly, it captures the often neglected region between linear and completely saturated behavior. Although constructed from disparate magnetic models, each with its own simplifying assumptions, our model is provably continuous, and the resulting torque and force equations are also continuous. We find that magnetic force can always be increased by increasing the directional derivatives in the applied field. However, there is an upper bound on the magnetic torque that can be generated, due to the shape and magnetic saturation. We provide a formula to compute the optimal applied-field direction to maximize torque for each applied-field magnitude. The simplicity of the presented model will facilitate real-time wireless control, as well as dynamic simulations, without the need for finite-element modeling.

Acknowledgment

The authors would like to thank Z. Nagy and K. Vollmers for their input.

References

[1] J. J. Abbott, Z. Nagy, F. Beyeler, and B. J. Nelson, "Robotics in the small, Part I: Microrobotics," *IEEE Robot. Autom. Mag.*, vol. 14, no. 2, pp. 92–103, Jun. 2007.
[2] K. B. Yesin, K. Vollmers, and B. J. Nelson, "Modeling and control of untethered biomicrorobots in a fluidic environment using electromagnetic fields," *Int. J. Robot. Res.*, vol. 25, no. 5/6, pp. 527–536, 2006.
[3] S. Martel, J.-B. Mathieu, O. Felfoul, A. Chanu, E. Aboussouan, S. Tamaz, and P. Pouponneau, "Automatic navigation of an untethered device in the artery of a living animal using a conventional clinical magnetic resonance imaging system," *Appl. Phys. Lett.*, vol. 90, no. 11, pp. 114105-1–114105-3, 2007.
[4] O. Ergeneman, G. Dogangil, M. P. Kummer, J. J. Abbott, M. K. Nazeeruddin, and B. J. Nelson, "A magnetically controlled wireless optical oxygen sensor for intraocular measurements," *IEEE Sensors J.*, to be published.
[5] K. Ishiyama, K. I. Arai, M. Sendoh, and A. Yamazaki, "Spiral-type micromachine for medical applications," *J. Micromechatron.*, vol. 2, no. 1, pp. 77–86, 2003.
[6] M. Gauthier and E. Piat, "An electromagnetic micromanipulation systems for single-cell manipulation," *J. Micromechatron.*, vol. 2, no. 2, pp. 87–119, 2004.
[7] M. B. Khamesee, N. Kato, Y. Nomura, and T. Nakamura, "Design and control of a microrobotic system using magnetic levitation," *IEEE/ASME Trans. Mechatron.*, vol. 7, no. 1, pp. 1–14, Mar. 2002.
[8] G. T. Gillies, R. C. Ritter, W. C. Broaddus, M. S. Grady, M. A. Howard, III, and R. G. McNeil, "Magnetic manipulation instrumentation for medical physics research," *Rev. Sci. Instrum.*, vol. 65, no. 3, pp. 533–562, 1994.
[9] D. C. Meeker, E. H. Maslen, R. C. Ritter, and F. M. Creighton, "Optimal realization of arbitrary forces in a magnetic stereotaxis system," *IEEE Trans. Magn.*, vol. 32, no. 2, pp. 320–328, Mar. 1996.
[10] S. O. Kasap, *Principles of Electronic Materials and Devices*, 2nd ed. New York: McGraw-Hill, 2002.
[11] D. Jiles, *Introduction to Magnetism and Magnetic Materials*. London, U.K.: Chapman and Hall, 1991.
[12] R. C. O'Handley, *Modern Magnetic Materials: Principles and Applications*. New York: Wiley, 2000.
[13] F. Amblard, B. Yurke, A. Pargellis, and S. Leibler, "A magnetic manipulator for studying local rheology and micromechanical properties of biological systems," *Rev. Sci. Instruments*, vol. 67, no. 3, pp. 818–827, 1996.
[14] R. M. Bozorth, *Ferromagnetism*. Princeton, NJ: Van Nostrand, 1951.
[15] B. D. Cullity, *Introduction to Magnetic Materials*. Reading, MA: Addison-Wesley, 1972.
[16] J. W. Judy, "Batch-fabricated ferromagnetic microactuators with silicon flextures" Ph.D. dissertation, Dept. Elect. Eng. Comput. Sci., Univ. California, Berkeley, 1996.
[17] M. Beleggia, M. De Graef, and Y. T. Millev, "The equivalent ellipsoid of a magnetized body," *J. Phys. D: Appl. Phys.*, vol. 39, pp. 891–899, 2006.
[18] J. A. Osborn, "Demagnetizing factors of the general ellipsoid," *Phys. Rev.*, vol. 67, no. 11/12, pp. 351–357, 1945.
[19] F. Bergmüller, C. Bärlocher, B. Geyer, M. Grieder, F. Heller, and P. Zweifel, "A torque magnetometer for measurements of the high-field anisotropy of rocks and crystals," *Meas. Sci. Technol.*, vol. 5, pp. 1466–1470, 1994.
[20] M. P. Kummer, J. J. Abbott, K. Vollmers, and B. J. Nelson, "Measuring the magnetic and hydrodynamic properties of assembled-MEMS microrobots," in *Proc. IEEE Int. Conf. Robot. Autom.*, 2007, pp. 1122–1127.

Convex Optimization Strategies for Coordinating Large-Scale Robot Formations

Jason C. Derenick and John R. Spletzer

Abstract—This paper investigates convex optimization strategies for coordinating a large-scale team of fully actuated mobile robots. Our primary motivation is both algorithm scalability as well as real-time performance. To accomplish this, we employ a formal definition from shape analysis for formation representation and repose the motion planning problem to one of changing (or maintaining) the shape of the formation. We then show that optimal solutions, minimizing either the total distance or minimax distance the nodes must travel, can be achieved through second-order cone programming techniques. We further prove a theoretical complexity for the shape problem of $O(m^{1.5})$ as well as $O(m)$ complexity in practice, where m denotes the number of robots in the shape configuration. Solutions for large-scale teams (1000's of robots) can be calculated in real time on a standard desktop PC. Extensions integrating both workspace and vehicle motion constraints are also presented with similar complexity bounds. We expect these results can be generalized for additional motion planning tasks, and will prove useful for improving the performance and extending the mission lives of large-scale robot formations as well as mobile ad hoc networks.

Index Terms—Barrier method, convex optimization, mobile ad hoc networks, optimal shape formation, second-order cone programming (SOCP), shape change.

I. Introduction

The robotics community has seen a tremendous increase in multiagent systems research in recent years. This has been driven in part by the maturation of the underlying technology: advances in embedded computing, sensor and actuator technology, and (perhaps most significantly) pervasive wireless communication. However, the primary motivation is the diverse range of applications envisaged for large-scale robot teams, defined herein as formations ranging from tens to